

# Josephson Junctions with Weak Links of Topological Crystalline Insulators

R. A. Snyder,<sup>1</sup> C. J. Trimble,<sup>1</sup> C. C. Rong,<sup>2</sup> P. A. Folkes,<sup>2</sup> P. J. Taylor,<sup>2</sup> and J. R. Williams<sup>1</sup>

<sup>1</sup>*Department of Physics, Joint Quantum Institute and the Center for Nanophysics and Advanced Materials, University of Maryland, College Park, MD 20742, USA*

<sup>2</sup>*Army Research Laboratory, Adelphi, MD 20783, USA*

(Dated: December 14, 2024)

We report on the fabrication of Josephson junctions using the topological crystalline insulator  $\text{Pb}_{0.5}\text{Sn}_{0.5}\text{Te}$  as the weak link. The properties of these junctions are characterized and compared to those fabricated with weak links of  $\text{PbTe}$ , a similar material yet topologically trivial. Most striking is the difference in the AC Josephson effect: junctions made with  $\text{Pb}_{0.5}\text{Sn}_{0.5}\text{Te}$  exhibit rich subharmonic structure consistent with a skewed current-phase relation. This structure is absent in junctions fabricated from  $\text{PbTe}$ . A discussion is given on the origin of this effect as an indication of novel behavior arising from the topologically nontrivial surface state.

Topological superconductors offer a new platform in which to study nontrivial ground states of matter. Since the early theoretical work of Read and Green [1], and Kitaev [2], there has been a rapid expansion in the number of topological systems that possess superconducting correlations. Key in the investigation of topological superconductors is the tantalizing prospect of the creation and manipulation of Majorana fermions – a particle possessing non-abelian statistics that may prove useful in quantum computation. Experimental work has focused on topological superconductors created from proximitized one-dimensional nanowires with strong spin-orbit interactions [3] and time-reversal invariant topological insulators with either intrinsic [4] or proximity-induced superconducting correlations [5–8]. Yet the list of possible topological superconductors does not end there and it is important to characterize these materials and elucidate the (potentially useful) differences therein.

Topological crystalline insulators (TCIs) produce topological states arising from the preservation of crystal symmetry [9]. One of the first theoretically predicted TCIs was  $\text{SnTe}$  and a band structure with 4 Dirac cones per unit cell was calculated (see the upper right inset of Fig. 1 for a diagram of the band structure) [10]. Soon after, experiments were able to demonstrate the topological nature of the surface state in  $\text{SnTe}$  and its cousin,  $\text{Pb}_{1-x}\text{Sn}_x\text{Te}$ , via angle-resolved photoelectron spectroscopy [11, 12] and scanning tunneling spectroscopy [13]. Important in these early experiments was the investigation of the topological phase transition in  $\text{Pb}_{1-x}\text{Sn}_x\text{Te}$  as a function of  $x$ : for values of  $x > 0.25$ , a topological surface state is observed [14]. For  $\text{PbTe}$ , a surface state was observed but without the topological properties measured in  $\text{Pb}_{1-x}\text{Sn}_x\text{Te}$  [14]. TCIs of  $\text{Pb}_{1-x}\text{Sn}_x\text{Te}$  have also been fabricated in thin film form, revealing both a thickness dependence of the topological phase and unique, electrically-tunable spin-filtered edge states [15]. More recently, theoretical investigations of the role of crystal symmetry in topological superconductors has begun. In particular, it was found that pairs of Majorana bound states can form and it was shown

that a new class of topological superconductor in TCI is possible [16, 17]. Experiments have shown superconductivity in In-doped  $\text{SnTe}$ , and odd-parity pairing indicative of a topological superconducting state has been observed [18]. Superconductivity has been induced by the proximity effect, and SQUID circuits from topological crystalline superconductors have been fabricated and conventional SQUID behavior has been measured [19] – a reminder that transport from the trivial bulk may mask any novel behavior of the surface state.

Here we report on the fabrication of Josephson junctions using both  $\text{Pb}_{1-x}\text{Sn}_x\text{Te}$  (topologically nontrivial)

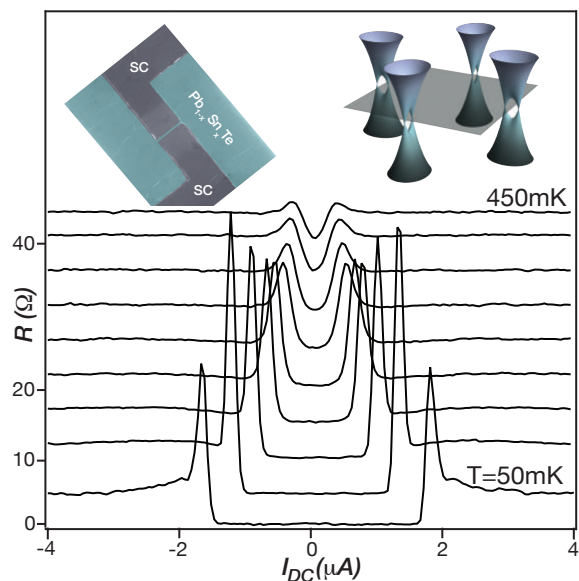


FIG. 1: Temperature dependence of the differential resistance  $R$ , where superconducting features appear below  $T=500$  mK. The peaks in  $R$  occur at values  $I_{DC} = I_C$ . (Inset, upper left) Scanning electron micrograph of the device similar to the ones studied in this Letter showing two superconducting (SC) aluminum leads (dark grey) and the TCI material  $\text{Pb}_{1-x}\text{Sn}_x\text{Te}$  (green). The spacing between the two SC leads is 100 nm. (Inset, upper right) Schematic of the band structure of  $\text{Pb}_{1-x}\text{Sn}_x\text{Te}$  where 4 Dirac cones appear across the  $\bar{X}$  point in k-space [10].

and PbTe (topological trivial) as a weak link material between the two aluminum leads. Characterization of these junctions is carried out, including measurements of (near) DC  $I - V$  curves, the  $I_C R_N$  product and its temperature dependence, magnetic diffraction pattern and the AC Josephson effect. The most striking deviation between the topologically-trivial and nontrivial junctions occurs under microwave radiation: in addition to the Shapiro steps observed at DC voltage values of  $nhf/2e$ , TCI Josephson junctions also exhibit steps at fractional values, indicating a strongly nonsinusoidal current-phase relation (CPR). The existence of higher harmonics in the CPR is confirmed through numerical simulations of the AC Josephson effect using a resistively-shunted junction model. The subharmonic structure reported here makes the topological superconducting state generated by proximity-induced superconductivity in TCIs distinct from prior measurements on other three dimensional topological insulator junctions, and we discuss the origin of this phenomena in terms of helical states predicted to exist in this material.

(111)  $\text{Pb}_{1-x}\text{Sn}_x\text{Te}$  epitaxial films were grown by molecular beam epitaxy (MBE) on semi-insulating GaAs substrates. The (111) orientation was selected for two reasons: it offers rich topological states on the surface that are symmetric with respect to the (110) mirror planes and it enables strain relaxation from dislocation glide along inclined (100) planes. The growth conditions were such that the surface adopts a simple  $(1 \times 1)$  re-

construction throughout growth as demonstrated by the RHEED pattern taken along the [110] azimuth [20]. The obtained compositions were either pure PbTe or nominally  $\text{Pb}_{0.5}\text{Sn}_{0.5}\text{Te}$  so as to facilitate discrimination between trivial insulator effects and TCI effects that emerge beyond the band inversion that is well known to occur in the neighborhood of  $\text{Pb}_{0.75}\text{Sn}_{0.25}\text{Te}$  [14]. In contrast to conventional MBE method that employs (PbTe, SnTe) compound sources, [21, 22] the composition of the materials of the present work was instead controlled using individual elemental sources (e.g., Pb, Sn and Te2) having  $>99.9999\%$  purity, and the surfaces were remarkably specular [20]. In depth information on the characterization of the material can be found in Ref. [20, 23].

Josephson junctions with a width of  $1\text{ }\mu\text{m}$  and length between 50 and 120 nm are patterned using electron-beam lithography. The deposition of the contacts forming the junction begins with an in-situ argon plasma etch for 60 secs at 50 W followed by sputtering of Ti/Al (3 nm/70 nm). During the deposition of the aluminum, the substrate is heated to  $100^\circ\text{C}$ , and it was found that the  $I_C R_N$  product of the junctions could be tuned from zero for room temperature deposition of the contacts to the value observed below [20]. After the superconducting layer is added,  $\text{Pb}_{1-x}\text{Sn}_x\text{Te}$  outside the junction is removed through a reactive ion etch of  $\text{Ar}/\text{H}_2$  (20:2) with a PMMA protective mask applied. An SEM image of a completed device is shown in the inset of Fig. 1. Devices are then cooled to temperatures down to 16mK and differential resistance  $R = dV/dI$  are measured in a current-bias configuration ( $I_{\text{bias}}$  between 1-10nA) with a lock-in amplifier. A total of 14 junctions showing superconducting properties were measured, two of which were investigated with the detail demonstrated in this Letter, each producing similar results [20]. Spectroscopy of the device is obtained by applying a DC current source ( $I_{\text{DC}}$ ) and plots of  $R$  vs.  $I_{\text{DC}}$  at different temperatures  $T$  are shown in Fig. 1. Peaks in  $R$  determine the values of the critical current  $I_{\text{DC}} = I_C$ , the critical current of the junction. The characteristic scale of the DC properties of the junction is given by  $I_C R_N$  ( $R_N$  is the normal state resistance of the junction), which rises from zero at  $T=500\text{mK}$  to  $\sim 10\text{ }\mu\text{V}$  at base temperature (Fig. 1).

Application of a perpendicular magnetic field  $B$  allows for a variation of the superconducting phase difference along the width of the junction. A plot of  $R$  as a function of  $I_{\text{DC}}$  and perpendicular magnetic field is shown in Fig. 2(a). In conventional junctions with a sinusoidal CPR and a uniform magnitude of the supercurrent across the device, a Fraunhofer pattern in the magnetic-field dependence of  $R$  is expected [24]. Importantly, Fraunhofer patterns or those resembling Fraunhofer patterns are experimentally useful for eliminating the possibility that the measured supercurrent in Fig. 1 arises from an electrical short between the superconducting leads, i.e. that the supercurrent is (at least approximately)

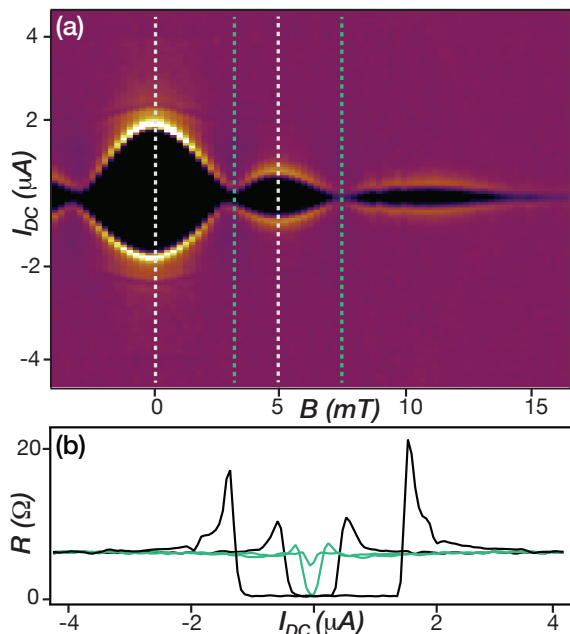


FIG. 2: (a) Plot of  $R(B, I_{\text{DC}})$  revealing a Fraunhofer-like pattern consistent with a (nearly) uniform supercurrent across the width of the device. (b) One-dimensional cuts in the data from (a) at  $B=0$ , 5.00 mT (black) and 2.75, 7.25 mT (red), where the latter two show the variation in  $R$  between one and two  $\Phi_0$  through the device.

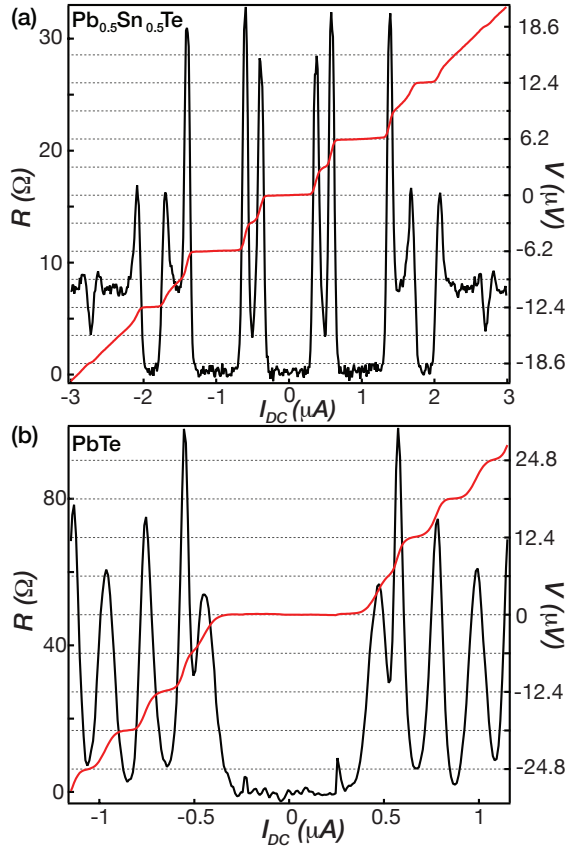


FIG. 3: A comparison of  $Pb_{0.5}Sn_{0.5}Te$  and  $PbTe$  at  $f=3$  GHz. (a) Plot of  $R$  showing minima at both expected values for Shapiro steps and at half integer values. Numerical integrated  $I-V$  data (red) shows Shapiro steps at  $nhf/2e=n*6.2\mu V$  and additional features at fractional values of  $1/2$  and  $3/2$ . (b) By comparison, a  $PbTe$  device showing only integer values of the Shapiro steps, both in  $R$  (black) and  $I-V$  (red), with an applied  $f$  of 3 GHz.

uniform over the width of the device. Fig. 2(a) has a pattern that is reminiscent of a Fraunhofer pattern with two important deviations: the width of the central lobe is roughly equal in width to the others and while  $I_C \rightarrow 0$  at  $B=2\Phi_0=7.25$  mT, it remains finite at  $B=\Phi_0=2.75$  mT. Cuts at  $B=2.75, 5.00$ , and  $7.25$  mT are compared with the  $B=0$  plot in Fig. 2(b). This deviation of the magnetic-field dependence from a Fraunhofer pattern is consistent with other 3D topological insulators [5, 6], and has been used in the past to imply a nonsinusoidal current-phase relations [25]. However, a simple modification to allow for the critical current density to smoothly vary along the width of the device can also produce a similar modification of the Fraunhofer pattern [20]. Hence, extraction of the current-phase relationship from measurements of this type can be tricky.

For a sinusoidal current-phase relation, a microwave voltage at frequency  $f$  applied to the junction produces steps in the  $I-V$  curves at voltages  $nhf/2e$  [26]. These steps will appear as minimum in the differential resistances  $R$ . Fig. 3(a) (black curve) shows  $R$  vs  $I_{DC}$  for

an applied microwave frequency of 3 GHz. Well-defined minimum of  $R$  are observed at values of  $nhf/2e$ .  $I-V$  curves are generated from a numeric integration of the differential resistance (See Supp Info to view measure DC  $I-V$  data, which also show fractional steps). The steps in  $I-V$  associated with these minimum in  $R$  are clearly seen in the generated  $I-V$  data [Fig 3(a) red], corresponding to steps of  $hf/2e=6.2\mu V$  and in agreement with expectations. Besides these pronounced minima are additional structure. Structure between the conventional minimum are associated with higher harmonics of the CPR and enabling the presence of fractional values of the AC Josephson effect. The integrated  $I-V$  shows a subharmonic feature at  $hf/4e$  and  $3hf/2e$ , demonstrating that a modification of the conventional  $\sin(\varphi)$  CPR is observed in these junctions.

To investigate whether these half plateau steps arise from any topological properties of the weak link material or simply from the presence of a surface state (which both  $PbTe$  and  $Pb_{1-x}Sn_xTe$  materials have), junctions were fabricated from the topologically-trivial material  $PbTe$ .  $R$  under 3 GHz radiation is shown in Fig. 3(b) (black curve), a conventional Shapiro step behavior exists, showing no structure in between plateaus. Also shown are the  $I-V$  curve (red) showing only plateaus at multiples of  $6.2\mu V$ , indicating that a current-phase relation arises primarily from a single frequency. Measurements of this junction at higher powers and frequencies show similar behavior: as a function of each only integer Shapiro steps are observed [20].

Further information on the CPR is revealed by a plot of the power dependence of the subharmonic structure. Fig. 4(a) is a plot of  $R$  for an the applied RF power  $P$  measured between -27.25 and -9 dBm taken at  $f=2.2$  GHz. Fundamental frequency Shapiro steps are seen (labeled by number in white) and follow a Bessel function power dependence, as expected [26]. In addition, subharmonic structure is observed in between the primary plateaus (along the vertical indicated by the white arrows) and different structure between different Shapiro steps. For example, a certain values of  $P$  a single dip is observed between steps 0 and 1, where two dips are seen between steps 3 and 4. This structure follows a more complicated pattern: as a function of power and  $I_{DC}$  one and sometimes two minima are seen. A one-dimensional cut of  $R$  Fig. 4(a) taken at  $P=-15$  dBm (grey line) demonstrates the intricate behavior observed in  $R$ . If only the fundamental and a second harmonic  $[I_S \propto \sin(\varphi) + \sin(2\varphi)]$ , only a strong, single dip in  $R$  would be present in between conventional Shapiro steps [20]. This is not the case.

To confirm that a current-phase relation possessing multiple harmonics can mimic the data of Fig. 4(a), we perform a numerical integration of the resistively shunted junction (RSJ) model [26] (see Ref. [20] for details of the simulations). As the data suggests, multiple harmonics are present. Theoretical predictions for either

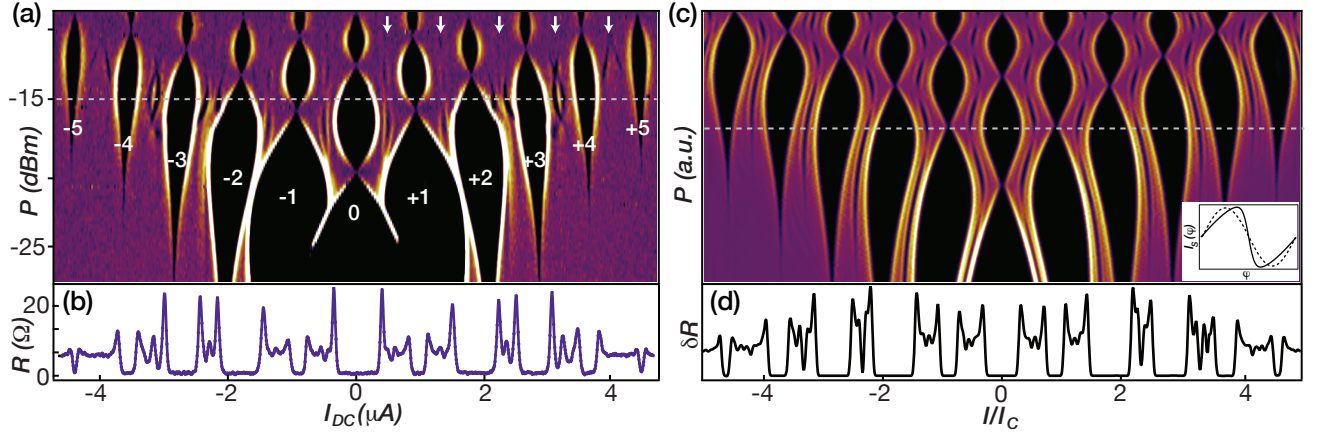


FIG. 4: (a) Power dependence of the AC Josephson effect taken at  $f=2.2$  GHz and applied power range -27.25 to 9 dBm. In addition to the main Shapiro steps observed (black regions indicated by white numbers), structure in between the primary steps is measured (along the vertical indicated by white arrows). (b) A cut of  $R$  taken along the grey line in Fig. 4(a). (c) Simulation of the RSJ model using a CPR for KO-2 theory for a ballistic Josephson junction, simulated over a similar range of parameters as the experimental data [Fig. 4(a)]. The saw-tooth behavior of the CPR is necessary to contain the higher harmonics in the CPS needed to mimic the experimental data. (Inset) A plot of the CPR for the KO-2 theory (solid line) is compared to a pure sine wave (dashed line). (d) A cut of the simulated differential resistance  $\delta R$  qualitatively reproduces that observed in the experiment.

highly transmitting [27] or ballistic junctions [28] offer saw-toothed shaped CPR, a shape which contains more than two harmonics. Fig. 4(c) is a simulation of the RSJ model using a current-phase relation

$$I_S = \frac{\pi\Delta}{eR_N} \sin(\varphi/2) \tanh \frac{\Delta \cos(\varphi/2)}{2k_B T}$$

[shown in the inset of Fig. 4(c), a CPR derived for Josephson junctions for ballistic weak links (KO-2 theory) [28] and using a ratio of  $\Delta$  to  $2k_B T$  of 5, consistent with the device under study. While not all the features are captured by the simulation, a side-by-side comparison of the one-dimensional cuts of the experimental data and the simulation [taken along the grey line of Fig. 4(c)] shows a qualitative agreement, reproducing the essential features of the subharmonic structure. The most important distinguishing features of this saw-toothed CPR are the appearance of peaks centered between successive integer Shapiro steps and the asymmetry of successive dips seen in the one-dimensional cut of the simulation [Fig. 4(d)]. These features are only observed in simulations with a strongly-skewed current-phase relation resulting from the existence of higher harmonics in  $I_S(\varphi)$  (see Ref [20] for simulations with other CPRs).

*Discussion.* Higher harmonics in the current-phase relation can arise for many reasons. What is significant here is the nonsinusoidal current-phase relation that are not observed other similar materials. Deviations from a sinusoidal CPR are neither observed in the topologically-trivial PbTe reported here nor in other three dimensional topological insulators. For example, in TI materials like  $\text{Bi}_2\text{Se}_3$  (another 3D TI), the AC Josephson effect has been studied and only integer Shapiro steps were ob-

served [6]. In addition, the CPR has been measured directly using a scanning SQUID and a sinusoidal CPR was reported [29]. Subharmonic Shapiro steps can arise from Josephson junctions with a sinusoidal relationship, but only in underdamped junctions (i.e. only in junctions with a large capacitance, which is not these case for the devices studied in this paper) [30].

A skewed current-phase relation is predicted for weak link junctions, both in the diffusive ( $L > \ell_e$ , where  $L$  is the length between the superconducting leads and  $\ell_e$  is the elastic scattering length) and the ballistic regime ( $L < \ell_e$ ). In the diffusive regime, the skewness only becomes significant at very low temperatures estimated to be below the temperature ranges studied here [20]. The plausibility of a purely ballistic junction is also ruled out from the estimation of  $\ell_e$  from magnetoresistance measurements [20].

In weak-link Josephson junctions where skewed a CPR and subharmonic structure have been seen are materials where the weak links been measured or are predicted to posses highly-transmitting modes. For example, a skewed current-phase relation and half-integer Shapiro have been observed recently in the one-dimensional materials like InAs nanowires [31, 32] and edge states of HgTe in the quantum spin Hall regime [33]. The origin of the this effect was linked to the highly-transmitting modes provided by the helical nature of the carriers in each of these materials arising from the coupling of spin to momentum. These results suggest that such a helical mode may also be present in TCI, which would account for the differences between PbTe and  $\text{Pb}_{0.5}\text{Sn}_{0.5}\text{Te}$  reported in this work. Helical states have been theoretically predicted to arise in TCIs as a result of disorder [10] and in materials with periodic strain [34], but these states



arise from different origins. Disorder breaks the crystalline symmetry protecting the topological phase, but opens gaps of opposite signs on the four Dirac cones. At the interface of regions with different gaps, a helical mode forms. In periodically strained TCIs, large pseudomagnetic fields are the sources of these helical modes. To disentangle the possible origin of highly-transmitting modes in our samples, phase coherent measurement of PbTe and  $\text{Pb}_{0.5}\text{Sn}_{0.5}\text{Te}$  were made. An equal magnitude of the weak anti-localization signal in each material [20] rules out the possibility of large pseudo magnetic fields [35], leaving disorder-induced helical modes a potential explanation for the highly-transmitting modes responsible for the nonsinusoidal CPR extracted here from the AC Josephson effect.

We thank Fred Wellstood for useful discussions and to Leo DiCarlo for assistance with measurements. This work was sponsored by the grants National Science Foundation Physics Frontier Center at the Joint Quantum Institute (PHY-1430094) and the Army Research Office (W911NF1710027).

- 
- [1] N. Read and D. Green, *Phys. Rev. B* **61**, 10267 (2000).
  - [2] A. Kitaev, *Phys.-Usp.* **44**, 131 (2001).
  - [3] V. Mourik, K. Zuo, S. M. Frolov, S. R. Plissard, E. P. A. M. Bakkers, L. P. Kouwenhoven, *Science* **336**, 1003 (2012).
  - [4] S. Sasaki, M. Kriener, K. Segawa, K. Yada, Y. Tanaka, M. Sato, and Y. Ando, *Phys. Rev. Lett.* **107**, 217001 (2011).
  - [5] J. R. Williams, A. J. Bestwick, P. Gallagher, Seung Sae Hong, Y. Cui, Andrew S. Bleich, J. G. Analytis, I. R. Fisher, and D. Goldhaber-Gordon, *Phys. Rev. Lett.* **109**, 056803 (2012).
  - [6] M. Veldhorst, M. Snelder, M. Hoek, T. Gang, V. K. Guduru, X. L. Wang, U. Zeitler, W. G. van der Wiel, A. A. Golubov, H. Hilgenkamp, and A. Brinkman, *Nature Mat.* **11**, 417 (2012).
  - [7] J. Wiedenmann, E. Bocquillon, R. S. Deacon, S. Hartinger, O. Herrmann, T. M. Klapwijk, L. Maier, C. Ames, C. Brüne, C. Gould, A. Oiwa, K. Ishibashi, S. Tarucha, H. Buhmann and L. W. Molenkamp, *Nature Comm.* **7**, 10303 (2016).
  - [8] R. S. Deacon, J. Wiedenmann, E. Bocquillon, F. Domínguez, T. M. Klapwijk, P. Leubner, C. Brüne, E. M. Hankiewicz, S. Tarucha, K. Ishibashi, H. Buhmann, and L. W. Molenkamp, *Phys. Rev. X* **7**, 021011 (2017).
  - [9] L. Fu, *Phys. Rev. Lett.* **106**, 106802 (2011).
  - [10] T. H. Hsieh, H. Lin, J. Liu, W. Duan, A. Bansil, and L. Fu, *Nature Comm.* **3**, 982 (2012).
  - [11] S.-Y. Xu, C. Liu, N. Alidoust, M. Neupane, D. Qian, I. Belopolski, Y. D. Denlinger, Y. J. Wang, H. Lin, L. A. Wray, G. Landolt, B. Slomski, J. H. Dil, A. Marcinkova, E. Morosan, Q. Gibson, R. Sankar, F. C. Chou, R. J. Cava, A. Bansil and M. Z. Hasan, *Nature Comm.* **3**, 1192 (2012).
  - [12] Y. Tanaka, Z. Ren, T. Sato, K. Nakayama, S. Souma, T. Takahashi, K. Segawa and Y. Ando, *Nature Phys.* **8**, 800 (2012).
  - [13] Y. Okada, M. Serbyn, H. Lin, D. Walkup, W. Zhou, C. Dhital, M. Neupane, S. Xu, Y. Jui Wang, R. Sankar, F. Chou, A. Bansil, M. Z. Hasan, S. D. Wilson, L. Fu, V. Madhavan, *Science* **341**, 1496 (2013).
  - [14] I. Zeljkovic, Y. Okada, M. Serbyn, R. Sankar, D. Walkup, W. Zhou, J. Liu, G. Chang, Y. J. Wang, M. Z. Hasan, F. Chou, H. Lin, A. Bansil, L. Fu and V. Madhavan, *Nature Mater.* **14**, 318 (2015).
  - [15] J. Liu, T. H. Hsieh, Peng Wei, W. Duan, J. Moodera, and L. Fu, *Nature Mater.* **13**, 178 (2014).
  - [16] X.-J. Liu, J. J. He, and K. T. Law, *Phys. Rev. B* **90**, 235141 (2014).
  - [17] C. Fang, M. J. Gilbert, and B. Andrei Bernevig, *Phys. Rev. Lett.* **112**, 106401 (2014).
  - [18] S. Sasaki, Z. Ren, A. A. Taskin, K. Segawa, L. Fu, and Yoichi Ando, *Phys. Rev. Lett.* **109**, 217004 (2012).
  - [19] R.-P. Klett, J. Schönle, A. Becker, D. Dyck, K. Rott, J. Haskenhoff, J. Krieff, T. Hübner, O. Reimer, C. Shekhar, J.-M. Schmalhorst, A. Hütten, C. Felser, W. Wernsdorfer, G. Reiss, arXiv:1706.10164 (2017).
  - [20] Additional information about the material synthesis, sample preparation, additional measurements and simulations will be given in the supplementary information at the time of publication.
  - [21] H. Holloway and J. N. Walpole, *Progress in Crystal Growth and Characterization*, **2**, 49 (1981).
  - [22] T. C. Harman, P. J. Taylor, M. P. Walsh, B. E. LaForge, *Science*, **297**, 2229 (2002).
  - [23] P. J. Taylor, P. Folkes, H. Hier, M. Graziano, R. A. Snyder, and J. R. Williams, *in preparation*.
  - [24] A. Barone, G. Paternò, *Physics and Applications of the Josephson Effect*. (Wiley-Interscience Publications, Canada 1982).
  - [25] C. Kurter, A. D. K. Finck, Y. S. Hor, and D. J. Van Harlingen, *Nature Comm.* **6**, 7130 (2014).
  - [26] K. K. Likharev, *Dynamics of Josephson Junctions and Circuits*. (Gordon and Breach Science Publishers, Amsterdam 1986).
  - [27] M. Titov and C. W. J. Beenakker, *Phys. Rev. B* **74**, 041401 (2006).
  - [28] K. K. Likharev, *Rev. Mod. Phys.* **51**, 101 (1979).
  - [29] I. Sochnikov, A. J. Bestwick, J. R. Williams, T. M. Lippman, I. R. Fisher, D. Goldhaber-Gordon, J. R. Kirtley, and K. A. Moler, *Nano Lett.* **13**, 3086 (2013).
  - [30] A. Valzadeh, M. R. Kolahchi, and J. P. Straley, *Journal of Nonlinear Mathematical Physics*, **15**, 407 (2008).
  - [31] T. Nishio, T. Kozakai, S. Amaha, M. Larsson, H. A. Nilsson, H. Q. Xu, G. Zhang, K. Tateno, H. Takayanagi and K. Ishibashi, *Nanotechnology* **22**, 445701 (2011).
  - [32] E. M. Spanton, M. Deng, S. Vaitieknas, P. Krogstrup, J. Nygård, C. M. Marcus and K. A. Moler, *Nature Phys.* Advanced Online Publication, <http://dx.doi.org/10.1038/nphys4224>.
  - [33] I. Sochnikov, L. Maier, C. A. Watson, J. R. Kirtley, C. Gould, G. Tkachov, E. M. Hankiewicz, C. Brune, H. Buhmann, L. W. Molenkamp and K. A. Moler *Phys. Rev. Lett.*, **114**, 066801 (2015).
  - [34] E. Tang and L. Fu, *Nature Phys.* **10**, 964 (2014).
  - [35] S. V. Morozov, K. S. Novoselov, M. I. Katsnelson, F. Schedin, L. A. Ponomarenko, D. Jiang, A. K. Geim, *Phys. Rev. Lett.*, **97**, 016801 (2006).